



science.scienmag.org/content/367/6475/285/suppl/DC1

Supplementary Material for **Singular charge fluctuations at a magnetic quantum critical point**

L. Prochaska, X. Li, D. C. MacFarland, A. M. Andrews, M. Bonta, E. F. Bianco,
S. Yazdi, W. Schrenk, H. Detz, A. Limbeck, Q. Si, E. Ringe, G. Strasser, J. Kono,
S. Paschen*

*Corresponding author. E-mail: paschen@ifp.tuwien.ac.at

Published 17 January 2020, *Science* **367**, 285 (2020)
DOI: 10.1126/science.aag1595

This PDF file includes:

Materials and Methods
Figs. S1 to S6
References

Materials and Methods

A. Growth of YbRh_2Si_2 thin films on Ge by molecular beam epitaxy

Whereas bulk poly- (35, 36) and single crystals (15, 37–40) of YbRh_2Si_2 have been synthesized by various techniques, the growth of thin films of this material has not been reported. Some bulk crystals, in particular with layered structures, can be lapped into thin samples, but for YbRh_2Si_2 thicknesses of about $10 \mu\text{m}$ reached by polishing down bulk single crystals are much larger than the limit of about 300 nm we estimate for THz transmission experiments on this compound. The bottom up growth of thin films is thus needed for our study.

The technique of choice is molecular beam epitaxy (MBE). We used a Riber Compact 21 MBE system with a growth chamber equipped with two Telemark electron beam evaporation sources for Rh (American Elements, 99.95%) and Si (Dr. Eberl MBE-Komponenten GmbH, resistivity $> 1000 \Omega\text{cm}$), and a low-temperature Knudsen cell for Yb (Ames Laboratory, 99.9%). Inficon quartz thickness monitors as well as a Hiden HAL 114-XBS RC mass spectrometer measure the deposition rates from the two electron beam sources independently. The Knudsen cell beam equivalent pressure is measured by a retractable ion gauge. The growth chamber is pumped to the low 10^{-10} torr range, as monitored by a chamber ion gauge. The total growth rate is limited to avoid (i) spitting behavior of the Rh target at higher powers and (ii) the full melting of the Si target in the carbon crucible because the solubility of carbon in liquid Si (41) would introduce impurities if the two were in direct contact.

To set the relative growth rates for achieving the correct 1:2:2 stoichiometry we used feedback from inductively-coupled plasma optical emission spectroscopy (Sect. B) on grown films. Typical growth conditions were beam equivalent pressures of 1.3×10^{-8} torr for Yb, and growth rates of 0.072 \AA/s for Si and 0.055 \AA/s for Rh as measured by the quartz monitors. Adjusted for the difference in distance to the substrate, this corresponds to a total growth rate of 13 nm/hr.

We selected Ge [fcc, $a = 5.658 \text{ \AA}$ (42)] as the substrate, because its nearest neighbor distance $a' = a\sqrt{2}/2 = 4.00081 \text{ \AA}$ has a lattice mismatch with the lattice parameter of YbRh_2Si_2 [$a = 4.011 \text{ \AA}$ (39)] of only a 0.25% (see Fig. 1A for a sketch of the matching) and because Ge is compatible with the targeted MBE growth conditions. A rough estimate of the critical thickness of the metastable regime, beyond which strained epitaxial layers may relax into a polycrystalline state, is determined by dividing the magnitude of the Burgers vector of the film, $|\vec{b}| = a/\sqrt{2}$, by the lattice mismatch (43, 44), yielding 111 nm. Up to this thickness, pseudomorphic growth of YbRh_2Si_2 on Ge(100) should thus be possible, which is suitable for our purpose.

3-inch epi-ready Ge substrates were cleaved into quarters and subjected to thermal oxide desorption at 500°C for 2 hours. Prior to each growth, the substrate and material sources were stabilized for a minimum of 2 hours. The growth temperature was 300°C as measured by a thermocouple positioned at the substrate heater.

B. Structural and analytical film characterization

High-resolution X-ray diffraction (HRXRD) with a PANalytical X’Pert system was performed on all films. The system was optimized around the Ge (004) peak and an $\omega - 2\theta$ scan was then recorded. The resulting scans (see Fig. 1B for a typical diffractogram) showed only a single phase in addition to the Ge substrate. The locations of the peaks associated with this phase correspond to the $(00l)$ peaks of YbRh_2Si_2 as expected for epitaxial film growth.

A LeBail analysis of the diffraction pattern revealed a lattice parameter $c = 9.8735 \text{ \AA}$ which is 0.1% larger than the literature data of $9.858 \text{ \AA} \leq c \leq 9.862 \text{ \AA}$ (45). This analysis was done with PANalytical’s HighScore Plus and is similar to a Rietveld refinement, taking into account only the peak positions and disregarding the intensities of the peaks.

The determination of the chemical composition of the films was accomplished by inductively coupled plasma optical emission spectroscopy (ICP-OES). The samples were cleaved

into multiple pieces to allow for the averaging of several runs, and each piece was fully dissolved in a mixture of nitric acid and 10% hydrofluoric acid for enough time to ensure that the film was dissolved. The prepared solutions were then diluted and measured in a Thermo Scientific iCAP 6500 RAD spectrometer. Liquid standards of the individual elements were prepared to calibrate the apparatus. The measured Yb:Rh:Si stoichiometry is 19.9:42.2:37.9 in at%, and 1:2.1:1.9 in atomic ratio. Due to the limited accuracy of this technique ($\pm 5\%$) this is consistent with a fully stoichiometric sample.

C. Transmission electron microscopy

Atomic resolution high-angle annular dark field scanning transmission electron microscopy (HAADF-STEM) images were acquired in a double aberration corrected FEI Titan Themis (S)TEM operated at 200 keV. The TEM specimen, with a thickness of less than 50 nm, was prepared using focused ion beam (FIB) milling. The technique of in-situ lift-out was applied in a FEI Helios DualBeam workstation. To minimize effects of the damage caused by the 30 keV Ga ion beam during the thinning process, the surfaces of the thinned sample were subsequently polished with a low-energy (2 keV) Ga ion beam.

The HAADF-STEM image (Fig. 1C) clearly shows high-quality epitaxial growth of the YbRh_2Si_2 film on the (45° rotated) Ge substrate. The HAADF signal is approximately proportional to atomic number square (Z^2), and therefore the Yb, Rh, Si, and Ge atomic columns are clearly distinguishable. The interface is remarkably sharp, with minimal (if any) atomic intermixing (Fig. 1D). The overlays shown in Fig. 1C demonstrate how perfectly the complex YbRh_2Si_2 lattice is formed. The visualizations of the crystal structures were prepared with VESTA 3 (46), which is provided free of charge for academic use.

D. Electrical resistivity

Electrical resistivity measurements were done in a Quantum Design PPMS Model 6000 system with ^3He option using the internal resistance bridge to measure the resistivity between 0.5 and 300 K using the van der Pauw technique. The low frequency (17 Hz) of the measurement ensures that these data represent the dc limit. Contacts were made by wire bonding of $25\ \mu\text{m}$ thick gold wires directly onto the film surface. A measurement current of $10\ \mu\text{A}$ was used and confirmed not to lead to self-heating at the lowest measurement temperatures.

E. THz time-domain transmission spectroscopy

In contrast to previous infrared optical conductivity studies that relied on reflection geometry measurements on bulk crystals and subsequent Kramers-Kronig (KK) transformation (20), we performed direct phase-resolved THz time-domain transmission spectroscopy measurements on MBE-grown YbRh_2Si_2 thin film samples, from which the real and imaginary part of the complex optical conductivity can be directly determined without making assumptions related to the KK relation.

The samples were mounted in a liquid He cryostat with a variable temperature range of 1.4 – 300 K. THz pulses were generated from a nonlinear (110) zinc telluride crystal pumped by a Ti:sapphire regenerative amplifier (1 kHz, 0.9 mJ, 775 nm, 200 fs, Clark-MXR, Inc., CPA-2001) via optical rectification. A small portion of the laser beam was split to form the probe path. The probe beam was delayed by a mechanical stage, and incident onto a piece of detection zinc telluride crystal together with the transmitted THz beam for probing the THz electric field via the electro-optic sampling method.

In the THz time-domain technique, the THz electric field measured as a function of time can provide both amplitude and phase information. Thus, for a thin film sample whose thickness is much smaller than the THz wavelength and skin depth, both the real (Fig. 3A) and the

imaginary part (Fig. S2) of the optical conductivity can be obtained. The real part is responsible for the THz wave attenuation whereas the imaginary part is typically interpreted as wave phase delay. In the thin film approximation, the complex optical conductivity of the thin film can be expressed as

$$\sigma = \frac{(1 + n_{\text{sub}})[1 - E_s(\omega)/E_{\text{ref}}(\omega)]Y_0}{d \cdot E_s(\omega)/E_{\text{ref}}(\omega)} \quad (\text{S1})$$

where n_{sub} is the refractive index of the substrate, ω is the THz angular frequency, $E_s(\omega)$ and $E_{\text{ref}}(\omega)$ are the Fourier-transformed frequency domain complex electric fields of the THz waves passing through the film on the substrate and through the bare substrate, respectively, Y_0 is the vacuum admittance, and d is thin film thickness.

In this limit, the real part $\text{Re}[\sigma(\omega)]$ is measured to higher accuracy than the imaginary part $\text{Im}[\sigma(\omega)]$, which is why we have focused on $\text{Re}[\sigma(\omega)]$ in the dynamical scaling analysis. Systematic errors on $\text{Im}[\sigma(\omega)]$ are due to the following effects: Firstly, because the film thickness is much smaller than the THz wavelengths, the phase shift of a transmitted THz wave is small. Secondly, the background lattice polarization of the sample is superimposed on the electronic response to give the total $\text{Im}[\sigma(\omega)]$. And finally, even small thickness differences between the sample substrate and the empty substrate used for reference measurements can lead to sizeable errors in $\text{Im}[\sigma(\omega)]$. Either of the latter two effects may be responsible for the negative values of $\text{Im}[\sigma(\omega)]$ we observe at the highest temperatures. By contrast, the $\text{Re}[\sigma(\omega)]$ data agree well with the dc electrical conductivity even at high temperatures, confirming that $\text{Re}[\sigma(\omega)]$ is robust against these effects.

Using $h\nu/(2\pi) \equiv k_B T$ to convert the energy of THz radiation into a thermal energy (47,48), our THz frequency range of 0.23 to 2.6 THz corresponds to 1.75 to 20 K. Our criterion for the low-frequency cutoff is that the incident THz signal must be at least two orders of magnitude larger than the noise floor. Our experiments probe YbRh_2Si_2 down to an effective minimum

energy scale $E_{\min} = \sqrt{(2\pi k_B T_{\min})^2 + (\hbar\omega_{\min})^2}$ that is a factor of 2.3 smaller than that reached in Ref. 20. Together with the high precision of our optical conductivity measurements, this allows for the robust quantum critical scaling analysis we have demonstrated here, which has remained elusive in previous investigations of heavy fermion bulk materials (49) and MBE-grown thin films (50–53).

F. Residual resistivity correction

For the dc resistivity $\rho(T)$, a subtraction of the residual resistivity can be readily done: The usual approach is to plot the resistivity on a T^α plot that stretches out the curve to a straight line (in the case of $\alpha = 1$, this is simply a linear-linear plot with $\rho = \rho_0 + A'T$). The residual resistivity ρ_0 can be read off such plots as the y -intercept. The basis for this assignment is Matthiessen's rule, which states that the residual scattering rate $1/\tau_{\text{res}}$ (due to static disorder or lattice defects) and the intrinsic scattering rate $1/\tau_{\text{in}}$ (that in YbRh_2Si_2 below about 15 K is dominated by quantum critical fluctuations) are additive.

To generalize the Matthiessen rule to the complex optical conductivity

$$\sigma(\omega, T) = \text{Re}[\sigma(\omega, T)] + i \text{Im}[\sigma(\omega, T)] \quad , \quad (\text{S2})$$

we suggest the form

$$\sigma_{\text{in}}^{-1}(\omega, T) = \sigma^{-1}(\omega, T) - \sigma_{\text{res}}^{-1}(\omega) \quad , \quad (\text{S3})$$

where the subscripts in and res denote intrinsic and residual, respectively. $\sigma_{\text{res}}^{-1}(\omega)$ is the finite-frequency generalization of the residual resistivity, for which we assume the Drude form

$$\sigma_{\text{res}}^{-1}(\omega) = \frac{1 - i\omega\tau_{\text{res}}}{\sigma_0} \quad \text{with} \quad \sigma_0 = \frac{ne^2\tau_{\text{res}}}{m} \quad (\text{S4})$$

that was shown to hold for the heavy fermion compound UPd_2Al_3 (50). For our critical scaling analysis of the intrinsic THz and dc data (Fig. 3B, and Fig. S5B on linear scales) with

$$\text{Re}[\sigma_{\text{in}}(\omega, T)] \cdot T^\alpha = f\left(\frac{\hbar\omega}{k_B T}\right) \quad (\text{S5})$$

we have used $\rho_0 = 11.6 \mu\Omega\text{cm}$ (i.e., $\sigma_0 = 8.62 \times 10^6 \Omega^{-1}\text{m}^{-1}$; see caption of Fig. 2) and $n = 2.6 \times 10^{28} \text{ m}^{-3}$ (7) as input parameters, and determined the mass enhancement m/m_0 (where m_0 is the free electron mass) as well as the power α of the scaling relationship. A contour plot of the normalized deviation is shown in Fig. S5A. The data scale best (i.e., show the minimal normalized deviation) at $m/m_0 \approx 130$ and $\alpha \approx 1$. The mass enhancement, that we attribute to the (non-critical) heavy fermion background contribution, is in good agreement with values estimated from an extended Drude analysis of far-infrared data of a bulk YbRh₂Si₂ single crystal (20). Importantly, the evidenced energy over temperature scaling, with a critical exponent $\alpha \approx 1$, is anchored by a simple fact: The inverse of the real part of the low-temperature intrinsic optical conductivity, $1/\text{Re}(\sigma_{\text{in}})$, is approximately linear in frequency (Fig. S4) just as its dc counterpart is approximately linear in temperature (Fig. 2B).

Finally, we inspect whether dynamical scaling is found also for the imaginary part of the optical conductivity, as expected from it being Kramers-Kronig related to the real part of the optical conductivity. As seen in Fig. S6, this is indeed the case. Best collapse is found for the exponent $\alpha = 1.16$, which is within about 10% of the value obtained when scaling the real part (Fig. 3); in view of the larger uncertainty/systematic errors of the imaginary part (see Sect. E for details) this agreement is satisfying, and demonstrates the internal consistency of our analysis.

Figures

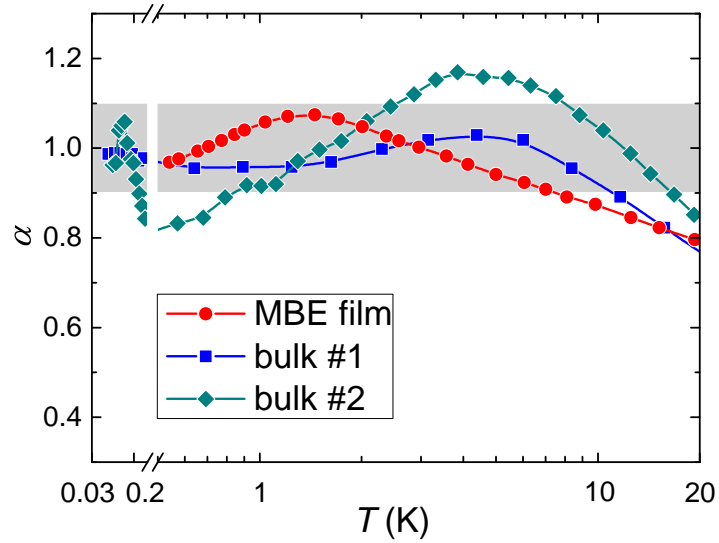


Figure S1: **Exponent from dc electrical resistivity of MBE-grown YbRh_2Si_2 .** Temperature-dependent exponent α , determined as $\partial \log(\rho - \rho_0)/\partial \log(T)$ for the two samples in Fig. 2, and an additional bulk single crystal (#2, $\rho_0 = 0.5 \mu\Omega\text{cm}$) (19) for comparison. The exponent approaches 1 in the low-temperature limit, but falls below 0.9 above about 8 K for our thin film, and above 11 and 16 K for the two different bulk single crystals (15, 19). Within the experimental error bar of $\Delta\alpha \approx 10\%$, all data points below 15 K fall in a zone of $\alpha = 1.0 \pm 0.1$ (grey shading).

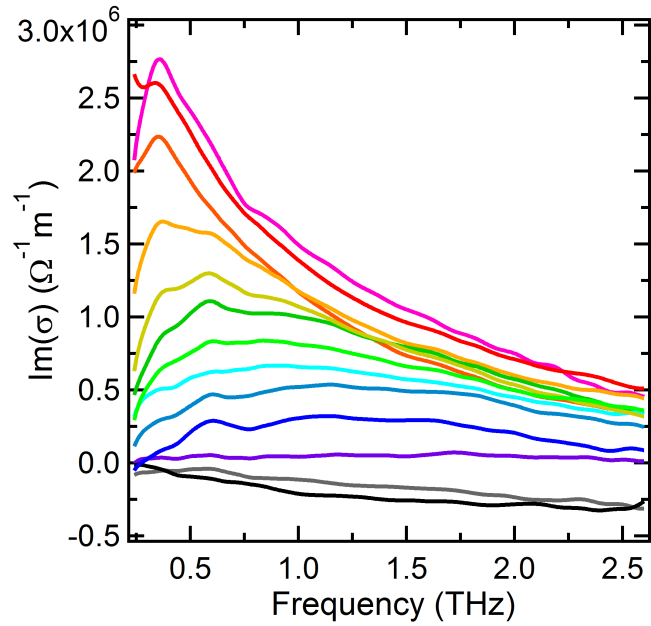


Figure S2: THz time-domain transmission spectroscopy of MBE-grown YbRh_2Si_2 . Imaginary part of optical conductivity, $\text{Im}(\sigma)$, vs frequency at different temperatures (bottom to top: 250, 150, 80, 60, 40, 30, 25, 20, 15, 10, 5, 3, 1.4 K). The strong temperature dependence, setting in below 80 K, echoes the behavior of $\text{Re}(\sigma)$ (Fig. 3A).

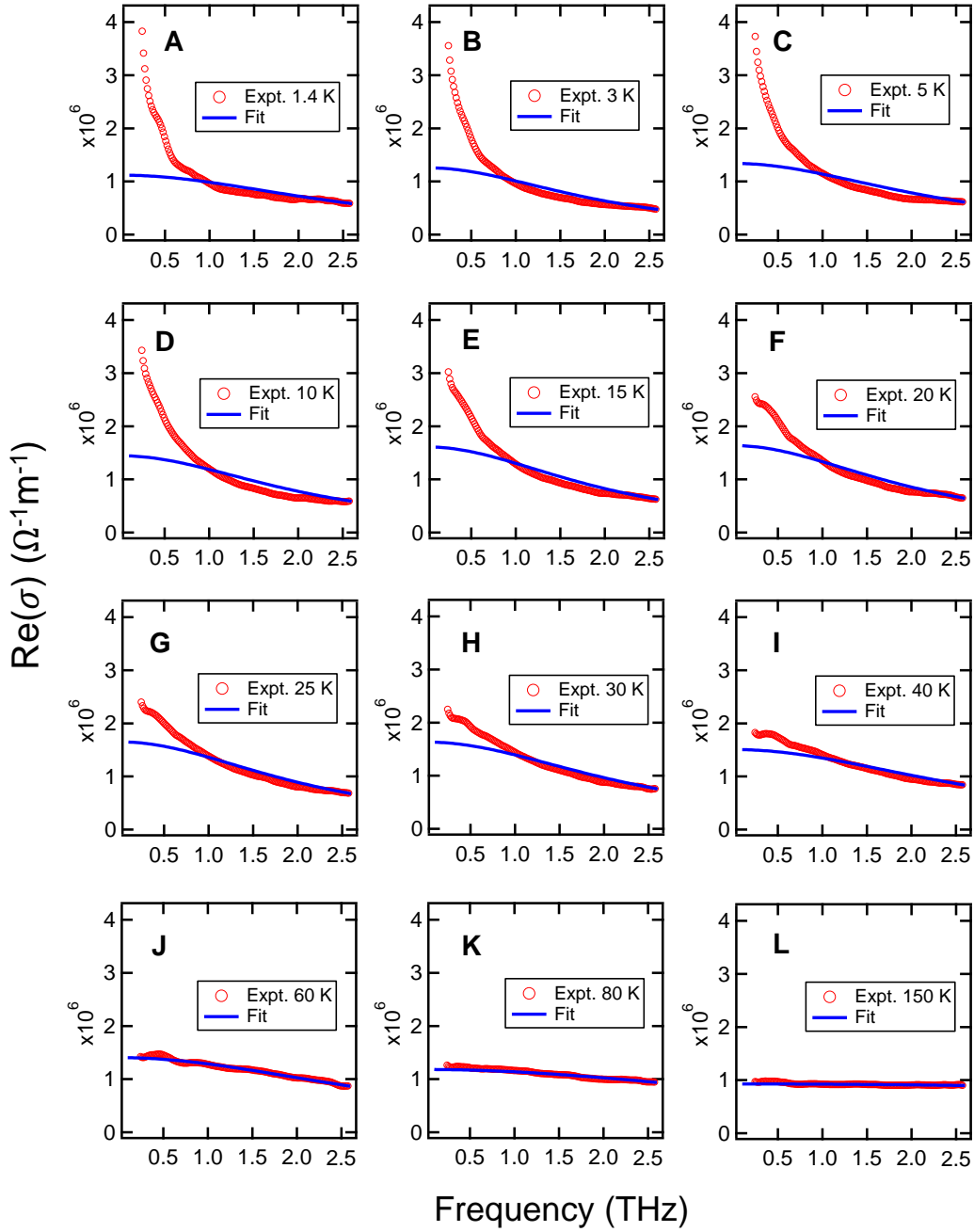


Figure S3: Non-Drude behavior of optical conductivity at low temperatures. $\text{Re}(\sigma)$ is well described by the Drude model only at high temperatures. Below 60 K, deviations appear at low frequencies and become increasingly pronounced with decreasing temperature. The fit was pinned to the data at the highest frequency, to illustrate the physically meaningful situation that the deviation develops at low frequencies. A fully free Lorentzian fit does not describe the data anywhere (neither at the low nor at the high frequency side; not shown).

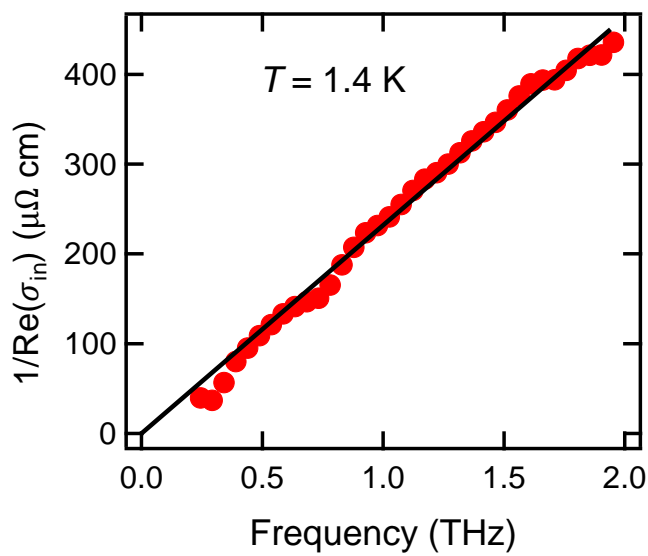


Figure S4: **Linear-in-frequency behavior of inverse real part of the intrinsic optical conductivity of MBE-grown YbRh_2Si_2 at the lowest temperature.** $1/\text{Re}(\sigma_{\text{in}})$ is approximately linear in frequency at 1.4 K, as seen by the good agreement between data (points) and a linear fit (line).

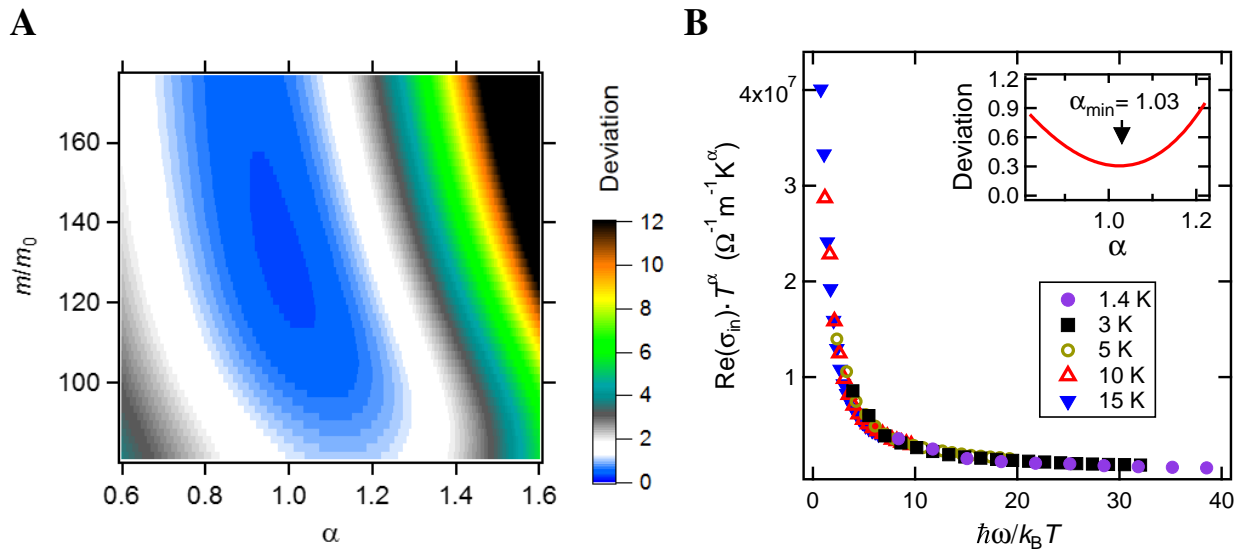


Figure S5: Scaling analysis of intrinsic optical conductivity of MBE-grown YbRh_2Si_2 . (A)
 Contour plot of the normalized deviation as function of the scaling exponent α and the mass enhancement m/m_0 of the Drude contribution due to the residual resistivity, used to determine α (and m/m_0) for optimum scaling. **(B)** ω/T scaling of Fig. 3B replotted on linear scales.

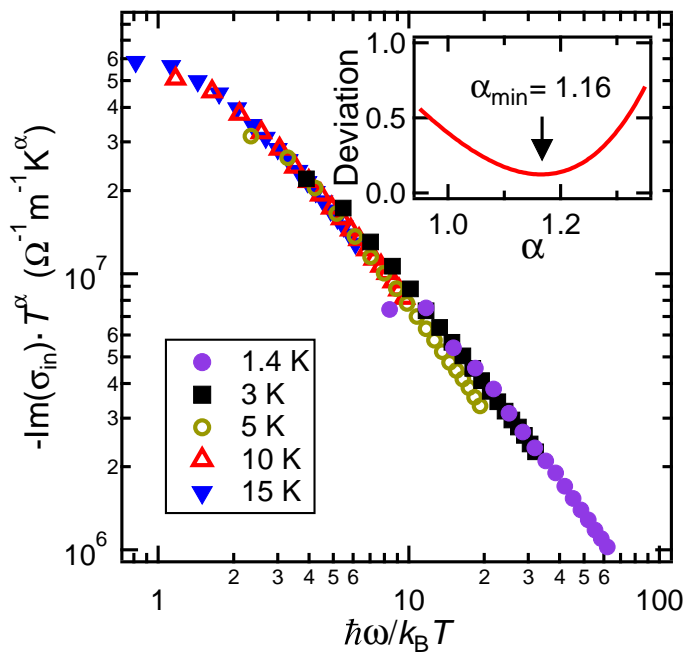


Figure S6: Scaling analysis of the imaginary part of the optical conductivity of MBE-grown YbRh_2Si_2 . The best scaling of $\text{Im}(\sigma_{\text{in}})$ is obtained for $\alpha = 1.16$, within about 10% of the value obtained for the scaling of $\text{Re}(\sigma_{\text{in}})$.

References and Notes

1. J. A. Hertz, Quantum critical phenomena. *Phys. Rev. B Condens. Matter* **14**, 1165–1184 (1976). [doi:10.1103/PhysRevB.14.1165](https://doi.org/10.1103/PhysRevB.14.1165) [Medline](#)
2. A. J. Millis, Effect of a nonzero temperature on quantum critical points in itinerant fermion systems. *Phys. Rev. B Condens. Matter* **48**, 7183–7196 (1993). [doi:10.1103/PhysRevB.48.7183](https://doi.org/10.1103/PhysRevB.48.7183) [Medline](#)
3. D. Bitko, T. F. Rosenbaum, G. Aeppli, Quantum critical behavior for a model magnet. *Phys. Rev. Lett.* **77**, 940–943 (1996). [doi:10.1103/PhysRevLett.77.940](https://doi.org/10.1103/PhysRevLett.77.940) [Medline](#)
4. P. Merchant, B. Normand, K. W. Krämer, M. Boehm, D. F. McMorrow, C. Rüegg, Quantum and classical criticality in a dimerized quantum antiferromagnet. *Nat. Phys.* **10**, 373–379 (2014). [doi:10.1038/nphys2902](https://doi.org/10.1038/nphys2902)
5. P. Giraldo-Gallo, J. A. Galvis, Z. Stegen, K. A. Modic, F. F. Balakirev, J. B. Betts, X. Lian, C. Moir, S. C. Riggs, J. Wu, A. T. Bollinger, X. He, I. Božović, B. J. Ramshaw, R. D. McDonald, G. S. Boebinger, A. Shekhter, Scale-invariant magnetoresistance in a cuprate superconductor. *Science* **361**, 479–481 (2018). [doi:10.1126/science.aan3178](https://doi.org/10.1126/science.aan3178) [Medline](#)
6. J. A. N. Bruin, H. Sakai, R. S. Perry, A. P. Mackenzie, Similarity of scattering rates in metals showing T-linear resistivity. *Science* **339**, 804–807 (2013). [doi:10.1126/science.1227612](https://doi.org/10.1126/science.1227612) [Medline](#)
7. S. Paschen, T. Lühmann, S. Wirth, P. Gegenwart, O. Trovarelli, C. Geibel, F. Steglich, P. Coleman, Q. Si, Hall-effect evolution across a heavy-fermion quantum critical point. *Nature* **432**, 881–885 (2004). [doi:10.1038/nature03129](https://doi.org/10.1038/nature03129) [Medline](#)
8. S. Friedemann, N. Oeschler, S. Wirth, C. Krellner, C. Geibel, F. Steglich, S. Paschen, S. Kirchner, Q. Si, Fermi-surface collapse and dynamical scaling near a quantum-critical point. *Proc. Natl. Acad. Sci. U.S.A.* **107**, 14547–14551 (2010). [doi:10.1073/pnas.1009202107](https://doi.org/10.1073/pnas.1009202107) [Medline](#)
9. J. Custers, K.-A. Lorenzer, M. Müller, A. Prokofiev, A. Sidorenko, H. Winkler, A. M. Strydom, Y. Shimura, T. Sakakibara, R. Yu, Q. Si, S. Paschen, Destruction of the Kondo effect in the cubic heavy-fermion compound Ce₃Pd₂₀Si₆. *Nat. Mater.* **11**, 189–194 (2012). [doi:10.1038/nmat3214](https://doi.org/10.1038/nmat3214) [Medline](#)
10. Y. Luo, L. Pourovskii, S. E. Rowley, Y. Li, C. Feng, A. Georges, J. Dai, G. Cao, Z. Xu, Q. Si, N. P. Ong, Heavy-fermion quantum criticality and destruction of the Kondo effect in a nickel oxypnictide. *Nat. Mater.* **13**, 777–781 (2014). [doi:10.1038/nmat3991](https://doi.org/10.1038/nmat3991) [Medline](#)
11. F. F. Balakirev, J. B. Betts, A. Migliori, S. Ono, Y. Ando, G. S. Boebinger, Signature of optimal doping in Hall-effect measurements on a high-temperature superconductor. *Nature* **424**, 912–915 (2003). [doi:10.1038/nature01890](https://doi.org/10.1038/nature01890) [Medline](#)
12. H. Oike, K. Miyagawa, H. Taniguchi, K. Kanoda, Pressure-induced Mott transition in an organic superconductor with a finite doping level. *Phys. Rev. Lett.* **114**, 067002 (2015). [doi:10.1103/PhysRevLett.114.067002](https://doi.org/10.1103/PhysRevLett.114.067002) [Medline](#)
13. S. Badoux, W. Tabis, F. Laliberté, G. Grissonnanche, B. Vignolle, D. Vignolles, J. Béard, D. A. Bonn, W. N. Hardy, R. Liang, N. Doiron-Leyraud, L. Taillefer, C. Proust, Change of

carrier density at the pseudogap critical point of a cuprate superconductor. *Nature* **531**, 210–214 (2016). [doi:10.1038/nature16983](https://doi.org/10.1038/nature16983) [Medline](#)

14. Y. Cao, V. Fatemi, S. Fang, K. Watanabe, T. Taniguchi, E. Kaxiras, P. Jarillo-Herrero, Unconventional superconductivity in magic-angle graphene superlattices. *Nature* **556**, 43–50 (2018). [doi:10.1038/nature26160](https://doi.org/10.1038/nature26160) [Medline](#)
15. O. Trovarelli, C. Geibel, S. Mederle, C. Langhammer, F. M. Grosche, P. Gegenwart, M. Lang, G. Sparn, F. Steglich, YbRh₂Si₂: Pronounced non-fermi-liquid effects above a low-lying magnetic phase transition. *Phys. Rev. Lett.* **85**, 626–629 (2000). [doi:10.1103/PhysRevLett.85.626](https://doi.org/10.1103/PhysRevLett.85.626) [Medline](#)
16. P. Gegenwart, J. Custers, C. Geibel, K. Neumaier, T. Tayama, K. Tenya, O. Trovarelli, F. Steglich, Magnetic-field induced quantum critical point in YbRh₂Si₂. *Phys. Rev. Lett.* **89**, 056402 (2002). [doi:10.1103/PhysRevLett.89.056402](https://doi.org/10.1103/PhysRevLett.89.056402) [Medline](#)
17. J. Orenstein, G. A. Thomas, A. J. Millis, S. L. Cooper, D. H. Rapkine, T. Timusk, L. F. Schneemeyer, J. V. Waszczak, Frequency- and temperature-dependent conductivity in YBa₂Cu₃O_{6+x} crystals. *Phys. Rev. B Condens. Matter* **42**, 6342–6362 (1990). [doi:10.1103/PhysRevB.42.6342](https://doi.org/10.1103/PhysRevB.42.6342) [Medline](#)
18. Materials and methods are available as supplementary materials.
19. T. Westerkamp, thesis, TU Dresden, Germany (2009).
20. S. Kimura, J. Sichelschmidt, J. Ferstl, C. Krellner, C. Geibel, F. Steglich, Optical observation of non-Fermi-liquid behavior in the heavy fermion state of YbRh₂Si₂. *Phys. Rev. B Condens. Matter* **74**, 132408 (2006). [doi:10.1103/PhysRevB.74.132408](https://doi.org/10.1103/PhysRevB.74.132408)
21. M. C. Aronson, R. Osborn, R. A. Robinson, J. W. Lynn, R. Chau, C. L. Seaman, M. B. Maple, Non-Fermi-liquid scaling of the magnetic response in UCu_{5-x}Pd_x(x=1,1.5). *Phys. Rev. Lett.* **75**, 725–728 (1995). [doi:10.1103/PhysRevLett.75.725](https://doi.org/10.1103/PhysRevLett.75.725) [Medline](#)
22. A. Schröder, G. Aeppli, R. Coldea, M. Adams, O. Stockert, H. v. Löhneysen, E. Bucher, R. Ramazashvili, P. Coleman, Onset of antiferromagnetism in heavy-fermion metals. *Nature* **407**, 351–355 (2000). [doi:10.1038/35030039](https://doi.org/10.1038/35030039) [Medline](#)
23. C. Stock, C. Broholm, F. Demmel, J. Van Duijn, J. W. Taylor, H. J. Kang, R. Hu, C. Petrovic, From incommensurate correlations to mesoscopic spin resonance in YbRh₂Si₂. *Phys. Rev. Lett.* **109**, 127201 (2012). [doi:10.1103/PhysRevLett.109.127201](https://doi.org/10.1103/PhysRevLett.109.127201) [Medline](#)
24. Q. Si, S. Rabello, K. Ingersent, J. L. Smith, Locally critical quantum phase transitions in strongly correlated metals. *Nature* **413**, 804–808 (2001). [doi:10.1038/35101507](https://doi.org/10.1038/35101507) [Medline](#)
25. P. Coleman, C. Pépin, Q. Si, R. Ramazashvili, How do Fermi liquids get heavy and die? *J. Phys. Condens. Matter* **13**, R723–R738 (2001). [doi:10.1088/0953-8984/13/35/202](https://doi.org/10.1088/0953-8984/13/35/202)
26. T. Senthil, M. Vojta, S. Sachdev, Weak magnetism and non-Fermi liquids near heavy-fermion critical points. *Phys. Rev. B Condens. Matter Mater. Phys.* **69**, 035111 (2004). [doi:10.1103/PhysRevB.69.035111](https://doi.org/10.1103/PhysRevB.69.035111)
27. D. van der Marel, H. J. A. Molegraaf, J. Zaanen, Z. Nussinov, F. Carbone, A. Damascelli, H. Eisaki, M. Greven, P. H. Kes, M. Li, Quantum critical behaviour in a high-*T_c* superconductor. *Nature* **425**, 271–274 (2003). [doi:10.1038/nature01978](https://doi.org/10.1038/nature01978) [Medline](#)

28. T. Senthil, Critical Fermi surfaces and non–Fermi liquid metals. *Phys. Rev. B Condens. Matter* **78**, 035103 (2008). [doi:10.1103/PhysRevB.78.035103](https://doi.org/10.1103/PhysRevB.78.035103)
29. H. Terletska, J. Vučićević, D. Tanasković, V. Dobrosavljević, Quantum critical transport near the Mott transition. *Phys. Rev. Lett.* **107**, 026401 (2011).
[doi:10.1103/PhysRevLett.107.026401](https://doi.org/10.1103/PhysRevLett.107.026401) [Medline](#)
30. T. Furukawa, K. Miyagawa, H. Taniguchi, R. Kato, K. Kanoda, Quantum criticality of Mott transition in organic materials. *Nat. Phys.* **11**, 221–224 (2015). [doi:10.1038/nphys3235](https://doi.org/10.1038/nphys3235)
31. H. Lee, J. P. Carini, D. V. Baxter, W. Henderson, G. Grüner, Quantum-critical conductivity scaling for a metal-insulator transition. *Science* **287**, 633–636 (2000).
[doi:10.1126/science.287.5453.633](https://doi.org/10.1126/science.287.5453.633) [Medline](#)
32. B. Keimer, J. E. Moore, The physics of quantum materials. *Nat. Phys.* **13**, 1045–1055 (2017).
[doi:10.1038/nphys4302](https://doi.org/10.1038/nphys4302)
33. P. T. Brown, D. Mitra, E. Guardado-Sánchez, R. Nourafkan, A. Reymbaut, C.-D. Hébert, S. Bergeron, A. S. Tremblay, J. Kokalj, D. A. Huse, P. Schauß, W. S. Bakr, Bad metallic transport in a cold atom Fermi-Hubbard system. *Science* **363**, 379–382 (2019).
[doi:10.1126/science.aat4134](https://doi.org/10.1126/science.aat4134) [Medline](#)
34. L. Prochaska, X. Li, D. C. MacFarland, A. M. Andrews, M. Bonta, E. F. Bianco, S. Yazdi, W. Schrenk, H. Detz, A. Limbeck, Q. Si, E. Ringe, G. Strasser, J. Kono, S. Paschen, Data for the publication “Singular charge fluctuations at a magnetic quantum critical point”. Zenodo (2019); doi:10.5281/zenodo.3541572.
35. D. Rossi, R. Marazza, R. Ferro, Ternary rme2x2 alloys of the rare earths with the precious metals and silicon (or germanium). *J. Less Common Met.* **66**, 17 (1979).
[doi:10.1016/0022-5088\(79\)90233-9](https://doi.org/10.1016/0022-5088(79)90233-9)
36. L. Gupta, *Theoretical and Experimental Aspects of Valence Fluctuations and Heavy Fermions* (Springer, 1987).
37. G. Knebel, R. Boursier, E. Hassinger, G. Lapertot, P. G. Niklowitz, A. Pourret, B. Salce, J. P. Sanchez, I. Sheikin, P. Bonville, H. Harima, J. Flouquet, Localization of 4f state in YbRh₂Si₂ under magnetic field and high pressure: Comparison with CeRh₂Si₂. *J. Phys. Soc. Jpn.* **75**, 114709 (2006). [doi:10.1143/JPSJ.75.114709](https://doi.org/10.1143/JPSJ.75.114709)
38. R. Hu, J. Hudis, C. Stock, C. Broholm, C. Petrovic, Single crystal growth of YbRh₂Si₂ using Zn flux. *J. Cryst. Growth* **304**, 114–117 (2007). [doi:10.1016/j.jcrysgro.2007.02.022](https://doi.org/10.1016/j.jcrysgro.2007.02.022)
39. C. Krellner, S. Taube, T. Westerkamp, Z. Hossain, C. Geibel, Single-crystal growth of YbRh₂Si₂ and YbIr₂Si₂. *Philos. Mag.* **92**, 2508–2523 (2012).
[doi:10.1080/14786435.2012.669066](https://doi.org/10.1080/14786435.2012.669066)
40. J.-P. Reid, M. A. Tanatar, R. Daou, R. Hu, C. Petrovic, L. Taillefer, Wiedemann-Franz law and nonvanishing temperature scale across the field-tuned quantum critical point of YbRh₂Si₂. *Phys. Rev. B Condens. Matter Mater. Phys.* **89**, 045130 (2014).
[doi:10.1103/PhysRevB.89.045130](https://doi.org/10.1103/PhysRevB.89.045130)
41. F. Durand, J. C. Duby, Carbon solubility in solid and liquid silicon—A review with reference to eutectic equilibrium. *J. Phase Equilibria* **20**, 61–63 (1999).
[doi:10.1361/105497199770335956](https://doi.org/10.1361/105497199770335956)

42. L. E. Vorobyev, in *Handbook Series on Semiconductor Parameters*, M. Levinstein, Ed. (World Scientific, 1996), pp. 33–57.
43. J. H. van der Merwe, Crystal interfaces. Part II. Finite overgrowths. *J. Appl. Phys.* **34**, 123–127 (1963). [doi:10.1063/1.1729051](https://doi.org/10.1063/1.1729051)
44. W. D. Callister, *Fundamentals of Materials Science and Engineering: An Interactive Text* (Wiley, ed. 5, 2000).
45. S. Wirth, S. Ernst, R. Cardoso-Gil, H. Borrmann, S. Seiro, C. Krellner, C. Geibel, S. Kirchner, U. Burkhardt, Y. Grin, F. Steglich, Structural investigations on YbRh_2Si_2 : From the atomic to the macroscopic length scale. *J. Phys. Condens. Matter* **24**, 294203 (2012). [doi:10.1088/0953-8984/24/29/294203](https://doi.org/10.1088/0953-8984/24/29/294203) [Medline](#)
46. K. Momma, F. Izumi, *VESTA 3* for three-dimensional visualization of crystal, volumetric and morphology data. *J. Appl. Cryst.* **44**, 1272–1276 (2011). [doi:10.1107/S0021889811038970](https://doi.org/10.1107/S0021889811038970)
47. R. N. Gurzhi, *Sov. Phys. JETP* **35**, 673 (1959).
48. C. Berthod, J. Mravlje, X. Deng, R. Žitko, D. van der Marel, A. Georges, Non-Drude universal scaling laws for the optical response of local Fermi liquids. *Phys. Rev. B Condens. Matter Mater. Phys.* **87**, 115109 (2013). [doi:10.1103/PhysRevB.87.115109](https://doi.org/10.1103/PhysRevB.87.115109)
49. L. Degiorgi, The electrodynamic response of heavy-electron compounds. *Rev. Mod. Phys.* **71**, 687–734 (1999). [doi:10.1103/RevModPhys.71.687](https://doi.org/10.1103/RevModPhys.71.687)
50. M. Scheffler, M. Dressel, M. Jourdan, H. Adrian, Extremely slow Drude relaxation of correlated electrons. *Nature* **438**, 1135–1137 (2005). [doi:10.1038/nature04232](https://doi.org/10.1038/nature04232) [Medline](#)
51. G. Bossé, L. S. Bilbro, R. V. Aguilar, L. D. Pan, W. Liu, A. V. Stier, Y. Li, L. H. Greene, J. Eckstein, N. P. Armitage, Low energy electrodynamics of the Kondo-lattice antiferromagnet CeCu_2Ge_2 . *Phys. Rev. B Condens. Matter Mater. Phys.* **85**, 155105 (2012). [doi:10.1103/PhysRevB.85.155105](https://doi.org/10.1103/PhysRevB.85.155105)
52. M. Scheffler, T. Weig, M. Dressel, H. Shishido, Y. Mizukami, T. Terashima, T. Shibauchi, Y. Matsuda, Terahertz conductivity of the heavy-fermion state in CeCoIn_5 . *J. Phys. Soc. Jpn.* **82**, 043712 (2013). [doi:10.7566/JPSJ.82.043712](https://doi.org/10.7566/JPSJ.82.043712)
53. G. Bossé, L. D. Pan, Y. S. Li, L. H. Greene, J. Eckstein, N. P. Armitage, Anomalous frequency and temperature-dependent scattering and Hund's coupling in the almost quantum critical heavy-fermion system CeFe_2Ge_2 . *Phys. Rev. B* **93**, 085104 (2016). [doi:10.1103/PhysRevB.93.085104](https://doi.org/10.1103/PhysRevB.93.085104)